Received: 17 September 2023 | Revised: 26 July 2024 | Accepted: 6 September 2024

DOI: 10.1002/nme.7598

RESEARCH ARTICLE

WILEY

Second-order computational homogenization of flexoelectric composites

Xiaoying Zhuang[1,2] | **Bin Li**[1,2,3] | **S. S. Nanthakumar**[2] | **Thomas Böhlke**[3]

[1]Department of Geotechnical Engineering, Tongji University, Shanghai, China

[2]Institute of Photonics, Department of Mathematics and Physics, Leibniz University Hannover, Hannover, Germany

[3]Institute of Engineering Mechanics, Karlsruhe Institute of Technology (KIT), Karlsruhe, Germany

Correspondence
Xiaoying Zhuang and Bin Li, Department of Geotechnical Engineering, Tongji University, Siping Road 1239, 200092 Shanghai, China.
Email: zhuang@iop.uni-hannover.de

Funding information
ERC Starting Grant, Grant/Award Number: 802205; Horizon2020

Abstract

Flexoelectricity shows promising applications for self-powered devices with its increased power density. This paper presents a second-order computational homogenization strategy for flexoelectric composite. The macro-micro scale transition, Hill–Mandel energy condition, periodic boundary conditions, and macroscopic constitutive tangents for the two-scale electromechanical coupling are investigated and considered in the homogenization formulation. The macrostructure and microstructure are discretized using C^1 triangular finite elements. The second-order multiscale solution scheme is implemented using ABAQUS with user subroutines. Finally, we present numerical examples including parametric analysis of a square plate with holes and the design of piezoelectric materials made of non-piezoelectric materials to demonstrate the numerical implementation and the size-dependent effects of flexoelectricity.

KEYWORDS

flexoelectricity, multiscale methods, second-order homogenization, size-dependent effects

1 | INTRODUCTION

Flexoelectricity—an electromechanical coupling between polarization and strain gradient-exists in all dielectric materials. Moreover, flexoelectricity is a size-dependent effect that becomes more significant in nanoscale systems.[1] These features make it different from piezoelectricity, which is induced polarization due to homogeneous strain. For an overview of flexoelectricity, readers are referred to the articles.[2–6]

The flexoelectric effect at the microscale has been exploited to design flexoelectric composites (piezoelectric metamaterials,[7] multiferroic composites,[8] etc.). The porous micro-structured materials were designed to generate an ultrahigh flexoelectric effect.[9] Moreover, the flexoelectric effect has long been regarded as a desirable property for advanced nano-/micro-electromechanical systems (N/MEMS) due to its universality and excellent scaling effect.[5] The homogenized electromechanical properties and multiscale modeling are very important, however not sufficient, for the analysis and design of the heterogeneous flexoelectric microstructure. A micromorphic approach for modeling the scale-dependent effects of flexoelectricity was presented by McBride et al.[10] The asymptotic expansion method was applied to derive effective coefficients of flexoelectric rods[11] and flexoelectric membranes.[12] The classic Eshelby's formalism was used for the homogenization of piezoelectric nanocomposites without using piezoelectric materials.[13] A variational approach of homogenization was developed towards piezoelectric and flexoelectric effective media.[14] A computational homogenization framework was proposed for the flexoelectric effect induced by heterogeneous piezoelectric phases,[15] and the method was combined with the topology optimization to enhance the flexoelectricity.[16,17]

The first-order computational homogenization method is a powerful approach to assess micro-macro structure-property relations,[18] where only the first gradient of the macroscopic displacement field is included. However, the uniformity assumption and neglect of geometrical size effects are the two major disadvantages of the first-order method, which significantly limit its applicability.[19] To overcome the concerns of the first-order homogenization method, the second-order computational homogenization method[20–23] has been developed, where the gradient of the macroscopic deformation gradient tensor is incorporated in the C^1-C^0 macro-micro scale transition. In this approach, C^1 continuous interpolations are applied at the macrolevel, while standard C^0 continuity is used for the discretization of the representative elementary volume (RVE) at the microlevel, so an additional integral condition on the fluctuation field at microlevel is required.[22]

The extension to second-order computational homogenization with the C^1-C^1 macro-micro scale transition has been proposed,[24,25] where the higher-order stress and strain tensors exist at both scales, and the homogenized stiffness tensors are calculated with the static condensation procedure. Due to the influence of strain gradient on material exhibiting flexoelectricity, the second-order homogenization method of C^1-C^1 macro-micro scale transition should be conducted. However, the static condensation procedure is not suitable for the electromechanical coupling problems, so perturbation analysis is instead used in this study. The global C^1 continuity for the discretization is required, and options include isogeometric analysis (IGA),[26,27] mixed FEM,[28–30] meshless methods,[31] and C^1 triangular elements.[32,33]

In this article, we develop a second-order homogenization method for flexoelectric composites accounting for size-dependent behavior. The homogenized electromechanical properties are computed by adopting the perturbation analysis. The C^1-C^1 micro-macro scale transition, periodic boundary conditions, and the Hill–Mandel energy condition are discussed. C^1 triangular element with 18 degrees of freedom per node is chosen for the discretization because of the ease of imposing periodic boundary conditions. The second-order homogenization scheme is implemented with the secondary development of ABAQUS.

The remainder of the article is organized as follows: Section 2 introduces the flexoelectricity theory; Section 3 presents the formulation of second-order computational homogenization; Section 4 describes the numerical implementation; Several numerical examples are illustrated in Section 5 and the conclusion derived from this work is presented in Section 6.

2 | FLEXOELECTRICITY THEORY

The electrical enthalpy density H and the internal energy U are often used for the variational formulation of flexoelectricity. The state variables and material parameters in the two formulations are discussed and compared at first.

Within the assumption of the linearized theory for dielectric solid, the electrical enthalpy density H can be written as.[34–37]

$$H = \frac{1}{2}c_{ijkl}\varepsilon_{ij}\varepsilon_{kl} + \frac{1}{2}b_{ijklmn}g_{ijk}g_{lmn} - e_{ijk}E_i\varepsilon_{jk} - f_{ijkl}E_ig_{jkl} - \frac{1}{2}\kappa_{ij}E_iE_j, \tag{1}$$

where ε_{ij}, g_{jkl}, E_i are the strain, strain-gradient, and electric field, respectively. They are defined as $\varepsilon_{ij} = \frac{1}{2}(u_{i,j} + u_{j,i})$, $g_{jkl} = u_{j,kl}$, and $E_i = -\phi_{,i}$, where $\boldsymbol{u}$ and ϕ are displacement vector and electric potential, respectively. c_{ijkl}, b_{ijklmn}, e_{ijk}, f_{ijkl} and κ_{ij} are the elastic, strain-gradient elastic, piezoelectric, flexoelectric and dielectric tensors, respectively.

While for the internal energy U based formulation for flexoelectricity, it is the function of strain, strain gradient, and polarization,[29]

$$U = \frac{1}{2}c_{ijkl}\varepsilon_{ij}\varepsilon_{kl} + \frac{1}{2}b_{ijklmn}g_{ijk}g_{lmn} + d_{ijk}P_i\varepsilon_{jk} + h_{ijkl}P_i\varepsilon_{jk,l} + \frac{1}{2}\alpha_{ij}P_iP_j, \tag{2}$$

where $U = H + E_iD_i$, d_{ijk}, h_{ijkl} and α_{ij} are the piezoelectric, flexoelectric, and reciprocal dielectric susceptibility tensors, respectively. The electric polarization $\boldsymbol{P}$ is introduced via the constitutive equation as[4]

$$P_i = \chi_{ij}E_j + e_{ijk}\varepsilon_{jk} + \mu_{ijkl}\varepsilon_{jk,l} = \chi_{ij}E_j + e_{ijk}\varepsilon_{jk} + f_{ijkl}u_{j,kl}, \tag{3}$$

where $\chi = \epsilon_0 \chi_e, \chi, \chi_e$ and ϵ_0 are the clamped dielectric susceptibility, electric susceptibility tensor and the permittivity of a vacuum, respectively. $\boldsymbol{f}$ and $\boldsymbol{\mu}$ are the flexoelectric coefficients corresponding to different descriptions of strain-gradient, and these two tensors are indirectly related due to the symmetry of the strain tensor.

It is worth noting that $\boldsymbol{e}$ and $\boldsymbol{\mu}$ are the coupling between the polarization and the strain and strain gradient, respectively, while $\boldsymbol{d}$ and $\boldsymbol{h}$ links the electric field to the strain and strain gradient, respectively.[34] The tensor $\boldsymbol{e}$, $\boldsymbol{\mu}$ and $\boldsymbol{\kappa}$ in Equations (1) and (3) are related to the tensor $\boldsymbol{d}$, $\boldsymbol{h}$ and $\boldsymbol{\alpha}$ of Equation (2) as[29,35]

$$d_{ijk} = \alpha_{im} e_{mjk}, \quad h_{ijkl} = \alpha_{im} \mu_{mjkl}, \quad \kappa_{ij} = \chi_{ij} + \epsilon_0 \delta_{ij} = 1/\alpha_{ij} + \epsilon_0 \delta_{ij}. \tag{4}$$

In this study, the electrical enthalpy density is adopted due to ease of application. For isotropic materials, the electrical enthalpy density can be written as[29]

$$\begin{aligned} H = {} & \frac{1}{2}\lambda \varepsilon_{ii}\varepsilon_{jj} + G\varepsilon_{ij}\varepsilon_{ij} + \frac{1}{2}l^2[\lambda g_{jij} g_{kik} + G(g_{ijk}g_{ijk} + g_{ijk}g_{jik})] - e_{ijk}E_i\varepsilon_{jk} \\ & - (f_1\delta_{ij}\delta_{kl} + f_2(\delta_{ik}\delta_{jl} + \delta_{il}\delta_{jk}))E_i g_{jkl} - \frac{1}{2}\kappa_{ij}E_iE_j, \end{aligned} \tag{5}$$

where λ and G are the Lamé parameters, l is the intrinsic length of material, f_1 and f_2 are the two independent flexoelectric constants of flexoelectric coefficient f_{ijkl}.

The corresponding constitutive equations are

$$\sigma_{ij} = \frac{\partial H}{\partial \varepsilon_{ij}} = 2G\varepsilon_{ij} + \lambda\varepsilon_{kk}\delta_{ij} - e_{kij}E_k, \tag{6}$$

$$\begin{aligned} \tau_{ijk} = {} & \frac{1}{2}\left(\frac{\partial H}{\partial g_{ijk}} + \frac{\partial H}{\partial g_{ikj}}\right) = \frac{1}{2}l^2[\lambda(g_{njn}\delta_{ik} + g_{nkn}\delta_{ij}) + G(2g_{ijk} + g_{jik} + g_{kij})] \\ & + f_1\delta_{jk}(-E_i) + f_2(\delta_{ij}(-E_k) + \delta_{ik}(-E_j)), \end{aligned} \tag{7}$$

$$D_i = -\frac{\partial H}{\partial E_i} = \kappa_{ij}E_j + e_{ijk}\varepsilon_{jk} + f_1 g_{ijj} + f_2(g_{jij} + g_{jji}) = P_i + \epsilon_0 E_i, \tag{8}$$

where σ_{ij}, τ_{ijk} and D_i are the stress, higher-order stress, and electric displacement, respectively.

The governing equations are given as[29,38]

$$(\sigma_{ij} - \tau_{ijk,k})_{,j} + f_i^b = 0 \quad \text{in} \quad \Omega, \tag{9}$$

$$D_{i,i} = \rho^f \quad \text{in} \quad \Omega, \tag{10}$$

where electrostatic stress and higher-order electric displacement are neglected, and f_i^b and ρ^f are body force and free charge on the solid body.

The boundary conditions are obtained as[28,29,38]

$$u_i = \bar{u}_i \quad \text{on} \quad \Gamma_u, \tag{11}$$

$$\phi = \overline{\phi} \quad \text{on} \quad \Gamma_\phi, \tag{12}$$

$$(\sigma_{ij} - \tau_{ijk,k})n_j + (D_l n_l)\tau_{ijk}n_k n_j - D_j(\tau_{ijk}n_k) = \bar{t}_i \quad \text{on} \quad \Gamma_t, \tag{13}$$

$$\tau_{ijk}n_j n_k = \bar{r}_i \quad \text{on} \quad \Gamma_r, \tag{14}$$

$$u_{i,k}n_k = \bar{v}_i \quad \text{on} \quad \Gamma_v, \tag{15}$$

$$D_i n_i = -\omega \quad \text{on} \quad \Gamma_D, \tag{16}$$

where $D_j = (\delta_{jk} - n_j n_k)\partial_k$ is the tangent gradient operator, and $\bar{t}_i, \bar{r}_i, \bar{v}_i$ and ω are surface traction, double traction, normal derivative of displacement, and surface charge density, respectively.

3 | SECOND-ORDER COMPUTATIONAL HOMOGENIZATION

3.1 | Macro-micro scale transition

The displacement and electric potential field are represented by a Taylor series expansion.[20]

$$\boldsymbol{u}_m = \boldsymbol{\varepsilon}_M \cdot \boldsymbol{x} + \frac{1}{2}\left[\boldsymbol{g}_M : (\boldsymbol{x} \otimes \boldsymbol{x})\right] + \boldsymbol{r}_u, \tag{17}$$

$$\phi_m = (-\boldsymbol{E}_M) \cdot \boldsymbol{x} + r_\phi, \tag{18}$$

where $\boldsymbol{\varepsilon} = (\boldsymbol{u} \otimes \nabla + \nabla \otimes \boldsymbol{u})/2$, $\boldsymbol{g} = (\boldsymbol{u} \otimes \nabla \otimes \nabla)$, and $\boldsymbol{E} = (-\phi\nabla)$. The subscript M denotes a macroscale quantity, while the subscript m denotes a microscale quantity. $\boldsymbol{x}$, $\boldsymbol{r}_u$, and r_ϕ are the microlevel spatial coordinate, the displacement microfluctuation field, and electric potential microfluctuation field, and the gradient of the electric field is ignored. The volume average of the strain and electric field at the microlevel are equal to the corresponding quantity at the macrostructural material point, as follows.

$$\frac{1}{V}\int_v \boldsymbol{\varepsilon}_m dv = \frac{1}{V}\int_v (\boldsymbol{u}_m \otimes \nabla) dv = \boldsymbol{\varepsilon}_M + \frac{1}{V}\int_v (\boldsymbol{g}_M \cdot \boldsymbol{x}) dv + \frac{1}{V}\int_V (\boldsymbol{r}_u \otimes \nabla) dv, \tag{19}$$

$$\frac{1}{V}\int_v \boldsymbol{g}_m dv = \frac{1}{V}\int_v (\boldsymbol{u}_m \otimes \nabla \otimes \nabla) dv = \boldsymbol{g}_M + \frac{1}{V}\int_v ((\boldsymbol{r}_u \otimes \nabla) \otimes \nabla) dv, \tag{20}$$

$$\frac{1}{V}\int_v (-\boldsymbol{E}_m) dv = \frac{1}{V}\int_v (\phi_m \nabla) dv = (-\boldsymbol{E}_M) + \frac{1}{V}\int_v (r_\phi \nabla) dv, \tag{21}$$

where the symmetric operator for computation of $\boldsymbol{\varepsilon}_m$ is dropped since it has been assumed according to Reference 20, and the minor symmetry $(\boldsymbol{g}_M)_{ijk} = (\boldsymbol{g}_M)_{ikj}$ has been used in Equation (19). The second term on the right side of Equation (19) $\frac{1}{V}\int_v (\boldsymbol{g}_M \cdot \boldsymbol{x}) dv$ should be zero, which indicates that the centroid of the RVE is at the origin of the coordinates. Thereby, the following equations can be obtained naturally from Equations (19)–(21).

$$\frac{1}{V}\int_v (\boldsymbol{r}_u \otimes \nabla) dv = \frac{1}{V}\int_\Gamma (\boldsymbol{r}_u \otimes \boldsymbol{n}) d\Gamma = \boldsymbol{0}, \tag{22}$$

$$\frac{1}{V}\int_v ((\boldsymbol{r}_u \otimes \nabla) \otimes \nabla)) dv = \frac{1}{V}\int_\Gamma ((\boldsymbol{r}_u \otimes \nabla) \otimes \boldsymbol{n}) d\Gamma = \boldsymbol{0}, \tag{23}$$

$$\frac{1}{V}\int_v (r_\phi \nabla) dv = \frac{1}{V}\int_\Gamma (r_\phi \boldsymbol{n}) d\Gamma = \boldsymbol{0}. \tag{24}$$

Therefore, due to the periodicity of RVE, the following boundary conditions can be obtained:

$$\boldsymbol{r}_{uR} = \boldsymbol{r}_{uL}, \quad \boldsymbol{r}_{uT} = \boldsymbol{r}_{uB}, \tag{25}$$

$$\boldsymbol{r}_{uR} \otimes \nabla = \boldsymbol{r}_{uL} \otimes \nabla, \quad \boldsymbol{r}_{uT} \otimes \nabla = \boldsymbol{r}_{uB} \otimes \nabla, \tag{26}$$

$$r_{\phi R} = r_{\phi L}, \quad r_{\phi T} = r_{\phi B}. \tag{27}$$

where R, L, T, and B represent right, left, top, and bottom boundary of RVE, respectively.

3.2 | The Hill–Mandel energy condition

Without considering the electric field gradient, the Hill–Mandel energy condition[39] can be expressed as

$$\frac{1}{V}\int_v (\boldsymbol{\sigma}_m : \delta\boldsymbol{\varepsilon}_m + \boldsymbol{\tau}_m \vdots \delta\boldsymbol{g}_m - \boldsymbol{D}_m \cdot \delta\boldsymbol{E}_m) dv = \boldsymbol{\sigma}_M : \delta\boldsymbol{\varepsilon}_M + \boldsymbol{\tau}_M \vdots \delta\boldsymbol{g}_M - \boldsymbol{D}_M \cdot \delta\boldsymbol{E}_M, \tag{28}$$

where $\boldsymbol{\sigma}$, $\boldsymbol{\tau}$, and $\boldsymbol{D}$ are the stress tensor, higher-order stress tensor, and electric displacement vector, respectively.

This condition can be subdivided into a mechanical and an electrical part as[40]

$$\frac{1}{V}\int_v (\boldsymbol{\sigma}_m : \delta\boldsymbol{\varepsilon}_m + \boldsymbol{\tau}_m \vdots\, \delta\boldsymbol{g}_m)dv = \boldsymbol{\sigma}_M : \delta\boldsymbol{\varepsilon}_M + \boldsymbol{\tau}_M \vdots\, \delta\boldsymbol{g}_M, \tag{29}$$

$$\frac{1}{V}\int_v (-\boldsymbol{D}_m \cdot \delta\boldsymbol{E}_m)dv = -\boldsymbol{D}_M \cdot \delta\boldsymbol{E}_M. \tag{30}$$

Substituting Equations (19) and (20) into the left side of Equation (29), we get

$$\begin{aligned}
&\frac{1}{V}\int_v (\boldsymbol{\sigma}_m : (\delta\boldsymbol{\varepsilon}_M + \delta\boldsymbol{g}_M \cdot \boldsymbol{x} + \delta\boldsymbol{r}_u \otimes \nabla) + \boldsymbol{\tau}_m \vdots\, (\delta\boldsymbol{g}_M + (\delta\boldsymbol{r}_u \otimes \nabla) \otimes \nabla))dv \\
&= \left(\frac{1}{V}\int_v \boldsymbol{\sigma}_m dv\right) : \delta\boldsymbol{\varepsilon}_M + \frac{1}{V}\int_v (\boldsymbol{\sigma}_m : (\delta\boldsymbol{r}_u \otimes \nabla))dv \\
&+ \left(\frac{1}{V}\int_v (\boldsymbol{\tau}_m + \boldsymbol{\sigma}_m \otimes \boldsymbol{x})dv\right) \vdots\, \delta\boldsymbol{g}_M + \frac{1}{V}\int_v (\boldsymbol{\tau}_m \vdots\, ((\delta\boldsymbol{r}_u \otimes \nabla) \otimes \nabla))dv.
\end{aligned} \tag{31}$$

To meet the Hill–Mandel condition (29), the integral terms containing microfluctuations should vanish:

$$\frac{1}{V}\int_v (\boldsymbol{\sigma}_m : (\delta\boldsymbol{r}_u \otimes \nabla))dv + \frac{1}{V}\int_v (\boldsymbol{\tau}_m \vdots\, ((\delta\boldsymbol{r}_u \otimes \nabla) \otimes \nabla))dv = 0. \tag{32}$$

The second term of Equation (32) can be written as

$$\frac{1}{V}\int_v (\boldsymbol{\tau}_m \vdots\, ((\delta\boldsymbol{r}_u \otimes \nabla) \otimes \nabla))dv = \frac{1}{V}\int_v ((\boldsymbol{\tau}_m : (\delta\boldsymbol{r}_u \otimes \nabla)) \cdot \nabla)dv - \frac{1}{V}\int_v ((\boldsymbol{\tau}_m \cdot \nabla) : (\delta\boldsymbol{r}_u \otimes \nabla))dv. \tag{33}$$

Therefore, substituting Equation (33) into Equation (32), we obtain:

$$\frac{1}{V}\int_v ((\boldsymbol{\sigma}_m - \boldsymbol{\tau}_m \cdot \nabla) : (\delta\boldsymbol{r}_u \otimes \nabla))dv + \frac{1}{V}\int_v ((\boldsymbol{\tau}_m : (\delta\boldsymbol{r}_u \otimes \nabla)) \cdot \nabla)dv = 0. \tag{34}$$

Using Gauss theorem, Equation (34) can be transformed into the following form containing the integral over the boundary of RVE,

$$\frac{1}{V}\int_{\Gamma} ((\boldsymbol{\sigma}_m - \boldsymbol{\tau}_m \cdot \nabla) \cdot \delta\boldsymbol{r}_u \cdot \boldsymbol{n})d\Gamma + \frac{1}{V}\int_{\Gamma} ((\boldsymbol{\tau}_m : (\delta\boldsymbol{r}_u \otimes \nabla)) \cdot \boldsymbol{n})d\Gamma = 0, \tag{35}$$

where Equation (35) can be approximately satisfied by applying the periodic conditions which will be discussed in Section 4.2 due to the periodicity assumption and the suppression of the corner microfluctuations.[24]

Similarly, the electrical part for the Hill–Mandel energy condition can be derived as follows. Substituting Equation (21) into the left side of Equation (30), we get

$$\frac{1}{V}\int_v (\boldsymbol{D}_m \cdot (\delta(-\boldsymbol{E}_M) + (\delta r_\phi \nabla))dv = \left(\frac{1}{V}\int_v \boldsymbol{D}_m dv\right) \cdot \delta(-\boldsymbol{E}_M) + \frac{1}{V}\int_v (\boldsymbol{D}_m \cdot (\delta r_\phi \nabla))dv. \tag{36}$$

The second term on the right-hand side of Equation (36) should be zero:

$$\frac{1}{V}\int_v (\boldsymbol{D}_m \cdot (\delta r_\phi \nabla))dv = \frac{1}{V}\int_v ((\delta r_\phi \boldsymbol{D}_m) \cdot \nabla)dv - \frac{1}{V}\int_v (\delta r_\phi (\boldsymbol{D}_m \cdot \nabla)) = \frac{1}{V}\int_{\Gamma} ((\delta r_\phi \boldsymbol{D}_m) \cdot \boldsymbol{n})d\Gamma = 0, \tag{37}$$

where $(\boldsymbol{D}_m \cdot \nabla) = 0$, as the free charge on the solid body is not considered in microscale. Equation (37) can also be satisfied due to the periodicity assumption.

According to Equations (31) and (36), the homogenized stresses and electric displacement can be derived as

$$\boldsymbol{\sigma}_M = \frac{1}{V}\int_v \boldsymbol{\sigma}_m dv, \tag{38}$$

TABLE 1 Loading cases for macroscopic constitutive tangents calculation.

Loading cases	S-1	S-2	S-3	S-4	S-5	S-6	S-7	S-8	S-9	S-10	S-11
ε_{11}	1	0	0	0	0	0	0	0	0	0	0
ε_{22}	0	1	0	0	0	0	0	0	0	0	0
ε_{12}	0	0	1	0	0	0	0	0	0	0	0
g_{111}	0	0	0	1	0	0	0	0	0	0	0
g_{112}	0	0	0	0	1	0	0	0	0	0	0
g_{122}	0	0	0	0	0	1	0	0	0	0	0
g_{211}	0	0	0	0	0	0	1	0	0	0	0
g_{212}	0	0	0	0	0	0	0	1	0	0	0
g_{222}	0	0	0	0	0	0	0	0	1	0	0
$-E_1$	0	0	0	0	0	0	0	0	0	1	0
$-E_2$	0	0	0	0	0	0	0	0	0	0	1

$$\boldsymbol{\tau}_M = \frac{1}{V}\int_v (\boldsymbol{\tau}_m + \boldsymbol{\sigma}_m \otimes \boldsymbol{x})dv, \tag{39}$$

$$\boldsymbol{D}_M = \frac{1}{V}\int_v \boldsymbol{D}_m dv. \tag{40}$$

3.3 | Macroscopic constitutive relations

In this work, we focus on the linear problem, and the macroscopic constitutive relations are given in incremental form from a general perspective. The updates of the macrolevel stress and electric displacement are performed by the following incremental relations

$$\Delta\boldsymbol{\sigma}_M = {}^4\boldsymbol{C}_{\sigma\varepsilon} : \Delta\boldsymbol{\varepsilon}_M + {}^5\boldsymbol{C}_{\sigma g} \,\vdots\, \Delta\boldsymbol{g}_M + {}^3\boldsymbol{C}_{\sigma E} \cdot \Delta(-\boldsymbol{E}_M), \tag{41}$$

$$\Delta\boldsymbol{\tau}_M = {}^5\boldsymbol{C}_{\tau\varepsilon} : \Delta\boldsymbol{\varepsilon}_M + {}^6\boldsymbol{C}_{\tau g} \,\vdots\, \Delta\boldsymbol{g}_M + {}^4\boldsymbol{C}_{\tau E} \cdot \Delta(-\boldsymbol{E}_M), \tag{42}$$

$$\Delta\boldsymbol{D}_M = {}^3\boldsymbol{C}_{D\varepsilon} : \Delta\boldsymbol{\varepsilon}_M + {}^4\boldsymbol{C}_{Dg} \,\vdots\, \Delta\boldsymbol{g}_M + {}^2\boldsymbol{C}_{DE} \cdot \Delta(-\boldsymbol{E}_M). \tag{43}$$

The homogenized stiffness matrices can be calculated with the perturbation analysis by solving linear equations for RVE, associated with incremental changes of macroscopic strains, strain gradients, and electric fields.[20] The multiple load cases for macroscopic constitutive relations are shown in Table 1. The load case is applied to the RVE with periodic boundary conditions, which will be illustrated in Section 4.2. Subsequently, we can compute the homogenized stresses and electric displacement according to Equations (38)–(40), and then obtain the macroscale constitutive relations with perturbation analysis. The so-called two-index notation is introduced to represent the homogenized constitutive tangents.

4 | NUMERICAL IMPLEMENTATION

4.1 | C^1 finite elements

C^1 finite elements, that were initially developed for modeling plate structures, are well suited to second-order homogenization of flexoelectricity. It is easier to impose the periodic boundary conditions due to the presence of displacement derivatives in the nodal degrees of freedom. A review and catalog of the C^1 finite elements can be found in Reference 41. The Argyris triangle[42] is a well-known h-version C^1 conforming element. The degrees of freedom include all second-order derivatives on vertices and normal derivatives at mid-side nodes (Figure 1), with complete fifth-order polynomial interpolation functions. However, the normal derivatives at midsides are undesirable and are eliminated by interpolating the

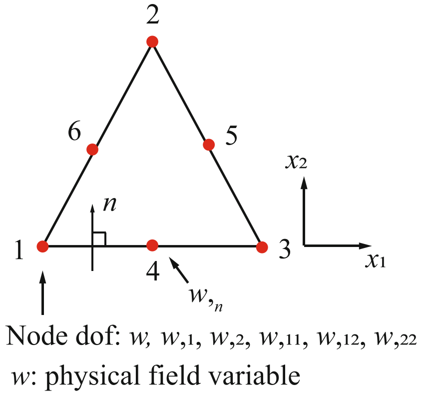

FIGURE 1 Argyris triangle.

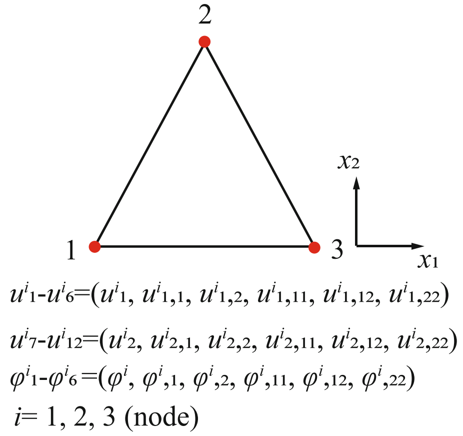

FIGURE 2 Bell triangle.

normal derivative at the mid-side nodes from the derivatives at the corner nodes, resulting in the C^1 Bell triangle element.[43] The displacement field still varies as a complete quintic inside the element, and the normal derivative along the edges of the element is constrained to be cubic.[44] The governing equation of flexoelectricity is a fourth-order partial differential equation, so the Bell triangle element satisfies the requirements of completeness and compatibility. The shape functions for the Bell triangle were given by Dasgupta and Sengupta.[33] The utility of the Bell triangle was proven in a series of studies on gradient elasticity problems.[44–46]

The Bell triangle is applied here as shown in Figure 2. Each node has eighteen degrees of freedom, which are displacement and electric potential and their first and second-order derivatives. The number of degrees of freedom for each element is 54, which is comparable to that in the mixed FEM method.[28,47] However, the Bell triangle eliminates the need for introducing Lagrange multipliers. Compared to the IGA method, there are significantly more degrees of freedom per node, but the IGA method faces challenges in establishing complex C^1 continuity models. Furthermore, the Bell triangle is more easily scalable in commercial software and offers convenience in imposing periodic boundary conditions.

In the absence of $E_{i,j}$, $\bar{r}_i$ and $\bar{v}_i$, the weak form of formulation for flexoelectricity is written as

$$\int_v(\boldsymbol{\sigma} : \delta\boldsymbol{\varepsilon} + \boldsymbol{\tau} \,\vdots\, \delta\mathbf{g} - \boldsymbol{D}\cdot\delta\boldsymbol{E})dv = \int_v(\boldsymbol{f}^b\cdot\delta\boldsymbol{u})dv + \int_{\Gamma_t}(\bar{\boldsymbol{t}}\cdot\delta\boldsymbol{u})d\Gamma - \int_v\rho^f\delta\phi dv - \int_{\Gamma_D}\omega\delta\phi d\Gamma. \tag{44}$$

The displacement $\boldsymbol{u}$ and electric potential ϕ fields, as well as their derivatives, can be approximated according to

$$\boldsymbol{u} = \mathbf{N}_u\boldsymbol{v}^e, \phi = \mathbf{N}_\phi\boldsymbol{\varphi}^e, \tag{45}$$

$$\boldsymbol{\varepsilon} = \boldsymbol{B}_u \boldsymbol{v}^e, \boldsymbol{g} = \boldsymbol{H}_u \boldsymbol{v}^e, -\boldsymbol{E} = \boldsymbol{B}_\phi \boldsymbol{\varphi}^e, \tag{46}$$

where $\boldsymbol{\varepsilon} = (\varepsilon_{11}, \varepsilon_{22}, \varepsilon_{12})^T$, $\boldsymbol{g} = (g_{111}, g_{112}, g_{122}, g_{211}, g_{212}, g_{222})^T$, $-\boldsymbol{E} = (-E_1, -E_2)^T$. $\boldsymbol{N}_u$, $\boldsymbol{N}_\phi$ are the shape function matrix, and $\boldsymbol{v}^e$ and $\boldsymbol{\varphi}^e$ are the nodal degrees of freedom. $\boldsymbol{B}_u$, $\boldsymbol{B}_\phi$, and $\boldsymbol{H}_u$ are matrices containing the gradient and Hessian of the corresponding shape functions.

Substituting Equations (45) and (46) into Equation (44) yields

$$\begin{bmatrix} \boldsymbol{K}_{uu} & \boldsymbol{K}_{u\phi} \\ \boldsymbol{K}_{\phi u} & \boldsymbol{K}_{\phi\phi} \end{bmatrix} \begin{bmatrix} \boldsymbol{v} \\ \boldsymbol{\varphi} \end{bmatrix} = \begin{bmatrix} \boldsymbol{F}_v \\ \boldsymbol{F}_\varphi \end{bmatrix}, \tag{47}$$

where

$$\boldsymbol{K}_{uu} = \sum_e \int_{v_e} (\boldsymbol{B}_u^T \boldsymbol{C} \boldsymbol{B}_u + l^2 \boldsymbol{H}_u^T \boldsymbol{Q} \boldsymbol{H}_u) dv, \tag{48}$$

$$\boldsymbol{K}_{u\phi} = \sum_e \int_{v_e} (\boldsymbol{B}_u^T \boldsymbol{e} \boldsymbol{B}_\phi + \boldsymbol{H}_u^T \boldsymbol{f}^T \boldsymbol{B}_\phi) dv, \tag{49}$$

$$\boldsymbol{K}_{\phi u} = \sum_e \int_{v_e} (\boldsymbol{B}_\phi^T \boldsymbol{e}^T \boldsymbol{B}_u + \boldsymbol{B}_\phi^T \boldsymbol{f} \boldsymbol{H}_u) dv, \tag{50}$$

$$\boldsymbol{K}_{\phi\phi} = \sum_e \int_{v_e} (\boldsymbol{B}_\phi^T (-\boldsymbol{\kappa}) \boldsymbol{B}_\phi) dv, \tag{51}$$

$$\boldsymbol{F}_u = \sum_e \int_{v_e} (\boldsymbol{N}_u^T \boldsymbol{f}^b) dv + \sum_e \int_{\Gamma_t} (\boldsymbol{N}_u^T \bar{\boldsymbol{t}}) d\Gamma, \tag{52}$$

$$\boldsymbol{F}_\phi = -\sum_e \int_{v_e} (\boldsymbol{N}_\phi^T \rho^f) dv - \sum_e \int_{\Gamma_D} (\boldsymbol{N}_\phi^T \omega) d\Gamma. \tag{53}$$

Moreover, $\boldsymbol{C}$, $\boldsymbol{Q}$, $\boldsymbol{\kappa}$, $\boldsymbol{e}$, and $\boldsymbol{f}$ can be written in matrix format as

$$\boldsymbol{C} = \begin{bmatrix} \lambda + 2G & \lambda & 0 \\ \lambda & \lambda + 2G & 0 \\ 0 & 0 & 4G \end{bmatrix}, \boldsymbol{\kappa} = \begin{bmatrix} \kappa_{11} & 0 \\ 0 & \kappa_{33} \end{bmatrix}, \tag{54}$$

$$\boldsymbol{e}^T = \begin{bmatrix} 0 & 0 & 2e_{15} \\ e_{31} & e_{33} & 0 \end{bmatrix}, \boldsymbol{f} = \begin{bmatrix} f_1 + 2f_2 & 0 & f_1 & 0 & 2f_2 & 0 \\ 0 & 2f_2 & 0 & f_1 & 0 & f_1 + 2f_2 \end{bmatrix}, \tag{55}$$

$$\boldsymbol{Q} = \begin{bmatrix} \lambda + 2G & 0 & 0 & 0 & \lambda & 0 \\ 0 & \lambda + 3G & 0 & G & 0 & \lambda \\ 0 & 0 & G & 0 & G & 0 \\ 0 & G & 0 & G & 0 & 0 \\ \lambda & 0 & G & 0 & \lambda + 3G & 0 \\ 0 & \lambda & 0 & 0 & 0 & \lambda + 2G \end{bmatrix}. \tag{56}$$

4.2 | Periodic boundary conditions

The twelve displacement-related degrees of freedom per node are expressed as $\boldsymbol{u}_g$ and the six electric potential-related degrees of freedom are denoted as $\boldsymbol{\phi}_g$. $\boldsymbol{u}_g$, and $\boldsymbol{\phi}_g$ of nodes on the RVE boundary can be rewritten into the matrix form as

$$\boldsymbol{u}_g = \boldsymbol{W} \boldsymbol{\varepsilon}_M + \boldsymbol{S} \boldsymbol{g}_M + \boldsymbol{r}_u, \tag{57}$$

$$\boldsymbol{\phi}_g = \boldsymbol{L}(-\boldsymbol{E}_M) + \boldsymbol{r}_\phi, \tag{58}$$

where

$$\boldsymbol{W}=\begin{bmatrix} x_1 & 0 & x_2 \\ 1 & 0 & 0 \\ 0 & 0 & 1 \\ 0 & 0 & 0 \\ 0 & 0 & 0 \\ 0 & 0 & 0 \\ 0 & x_2 & x_1 \\ 0 & 0 & 1 \\ 0 & 1 & 0 \\ 0 & 0 & 0 \\ 0 & 0 & 0 \\ 0 & 0 & 0 \end{bmatrix}, \boldsymbol{S}=\begin{bmatrix} \frac{1}{2}x_1^2 & x_1x_2 & \frac{1}{2}x_2^2 & 0 & 0 & 0 \\ x_1 & x_2 & 0 & 0 & 0 & 0 \\ 0 & x_1 & x_2 & 0 & 0 & 0 \\ 1 & 0 & 0 & 0 & 0 & 0 \\ 0 & 1 & 0 & 0 & 0 & 0 \\ 0 & 0 & 1 & 0 & 0 & 0 \\ 0 & 0 & 0 & \frac{1}{2}x_1^2 & x_1x_2 & \frac{1}{2}x_2^2 \\ 0 & 0 & 0 & x_1 & x_2 & 0 \\ 0 & 0 & 0 & 0 & x_1 & x_2 \\ 0 & 0 & 0 & 1 & 0 & 0 \\ 0 & 0 & 0 & 0 & 1 & 0 \\ 0 & 0 & 0 & 0 & 0 & 1 \end{bmatrix}, \boldsymbol{L}=\begin{bmatrix} x_1 & x_2 \\ 1 & 0 \\ 0 & 1 \\ 0 & 0 \\ 0 & 0 \\ 0 & 0 \end{bmatrix}. \tag{59}$$

Here x_1 and x_2 denote the coordinates of the node. Using the periodicity according to relations (25)–(27) leads to the equations

$$\boldsymbol{u}_{gR}-\boldsymbol{u}_{gL}=(\boldsymbol{W}_R-\boldsymbol{W}_L)\boldsymbol{\varepsilon}_M+(\boldsymbol{S}_R-\boldsymbol{S}_L)\boldsymbol{g}_M, \boldsymbol{u}_{gT}-\boldsymbol{u}_{gB}=(\boldsymbol{W}_T-\boldsymbol{W}_B)\boldsymbol{\varepsilon}_M+(\boldsymbol{S}_T-\boldsymbol{S}_B)\boldsymbol{g}_M, \tag{60}$$

$$\boldsymbol{\phi}_{gR}-\boldsymbol{\phi}_{gL}=(\boldsymbol{L}_R-\boldsymbol{L}_L)(-\boldsymbol{E}_M), \boldsymbol{\phi}_{gT}-\boldsymbol{\phi}_{gB}=(\boldsymbol{L}_T-\boldsymbol{L}_B)(-\boldsymbol{E}_M). \tag{61}$$

The above periodic condition can be called the gradient generalized periodic condition (PBC).[24] There is another boundary condition-gradient displacement periodic condition (DBC), where microfluctuations on the RVE boundaries are suppressed, so the displacement and electric potential field of nodes on the RVE boundary are then written as

$$\boldsymbol{u}_g=\boldsymbol{W}\boldsymbol{\varepsilon}_M+\boldsymbol{S}\boldsymbol{g}_M, \tag{62}$$

$$\boldsymbol{\phi}_g=\boldsymbol{L}(-\boldsymbol{E}_M). \tag{63}$$

4.3 | The second-order multiscale solution scheme

The second-order multiscale solution scheme is shown in Figure 3. The second-order homogenization procedure for flexoelectricity is implemented with ABAQUS. C^1 triangular finite element is realized using the user element subroutine UEL, and user subroutine UVARM with "dummy" elements are used for postprocessing the field results of user-defined elements. The field results are obtained as output in TECPLOT format for visualization. As user subroutine UVARM cannot be used with linear perturbation procedure in ABAQUS, the macroscopic constitutive tangents are calculated with perturbation analysis in the general step. The periodic boundary conditions are imposed with linear constraint equations in ABAQUS. As this study is on flexoelectric structures under small elastic deformation, the macro-micro scale transition (Figure 4) is carried out only once.

5 | NUMERICAL EXAMPLES

5.1 | Material equivalent parameter analysis of a square plate with holes

For the sake of comparison, only the representative material equivalent parameters of the flexoelectric microstructure are analyzed, and the equivalent parameters in the following examples are all expressed by the two-index notation. Taking the square plate with holes as an example, the effects of intrinsic length, microscale model size, porosity, and void distribution

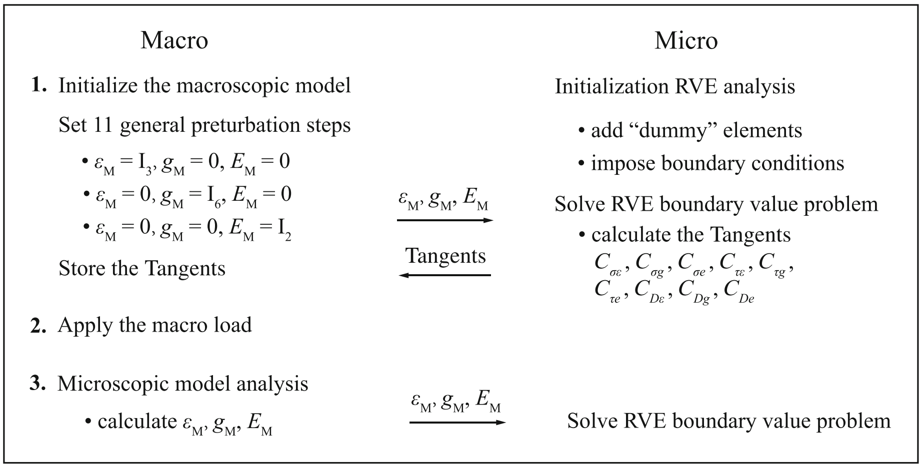

FIGURE 3 The second-order multiscale solution scheme.

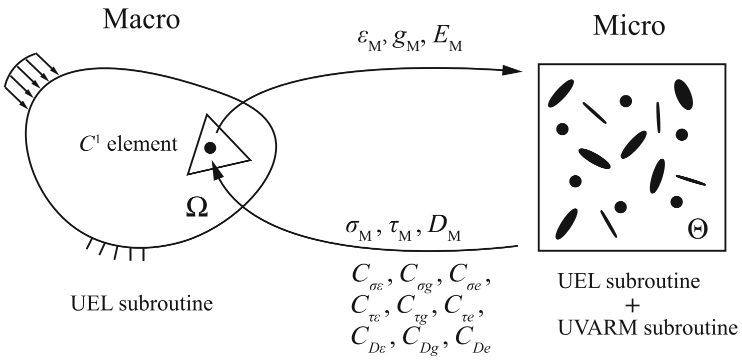

FIGURE 4 The macro-micro scale transition.

TABLE 2 Material properties ($[\lambda, G]$ = GPa, $[e] = \mathrm{C/m^2}$, $[\kappa]$ = nC/Vm, $[f] = \mu$C/m).

λ	G	e_{31}	e_{33}	e_{15}	k_{11}	k_{33}	f_1	f_2
179	54	−2.7	3.65	21.3	12.5	14.4	1	1

on the equivalent parameters are investigated. Furthermore, two different boundary conditions (PBC and DBC) are also compared. The material properties of microscale structure are listed in Table 2 based on.[27,28]

5.1.1 | The effects of intrinsic length and microscale model size

The expression of intrinsic length can be given by the self-consistent estimate[48] and its calculation is beyond the scope of this article. The intrinsic length in flexoelectricity analysis is taken as the model size multiplied by a factor smaller than one,[28,29] but the value of the factor is not definite.

The microscale model with a side length of 1 μm is shown in Figure 5. The effects of intrinsic length on the equivalent parameters of microstructure under PBC are shown in Figure 6. The parameters are normalized by dividing the corresponding material property in Table 2 to aid comparison. One can observe that the dielectric and flexoelectric coefficients decrease and the elastic and piezoelectric coefficients increase with the increase of intrinsic length, while all the coefficients remain unchanged when the intrinsic length is over 0.5 μm. The effects of boundary conditions, that is PBC and DBC, on the results are shown in Figure 7. The equivalent elastic coefficients remain quite similar irrespective

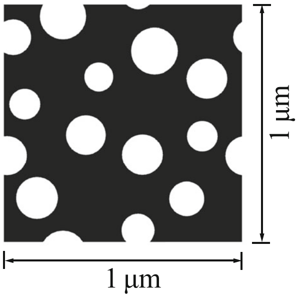

FIGURE 5 The mircroscale model with holes.

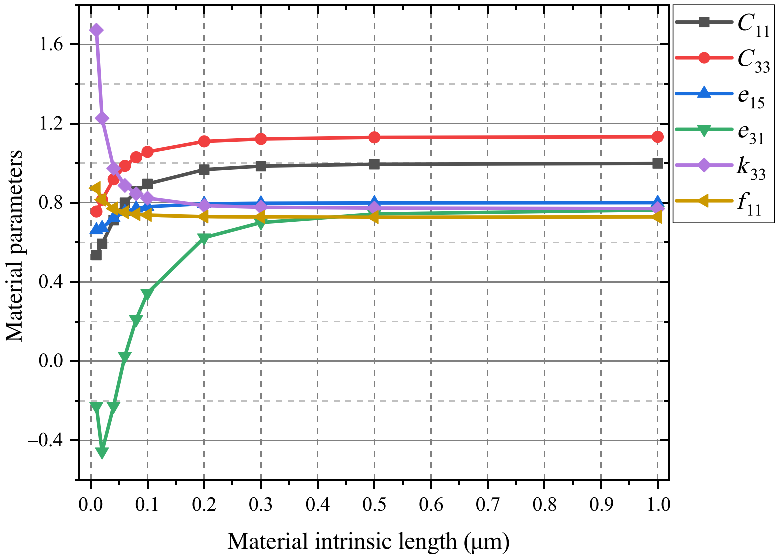

FIGURE 6 Material parameters of different intrinsic length l.

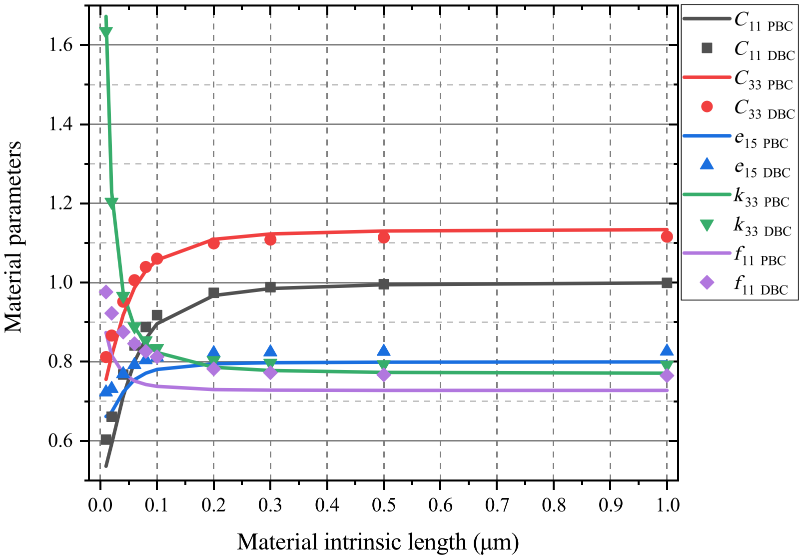

FIGURE 7 Material parameters of different intrinsic length l with different boundary conditions.

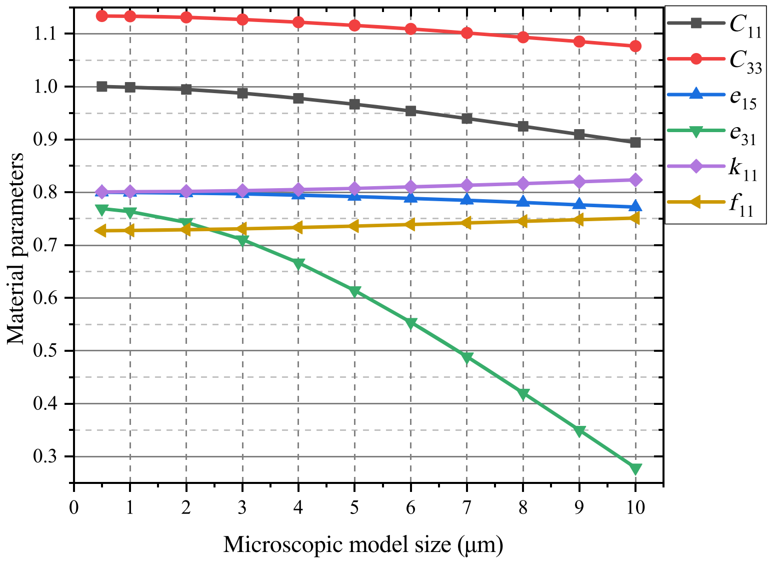

FIGURE 8 Material parameters of different microscopic model sizes.

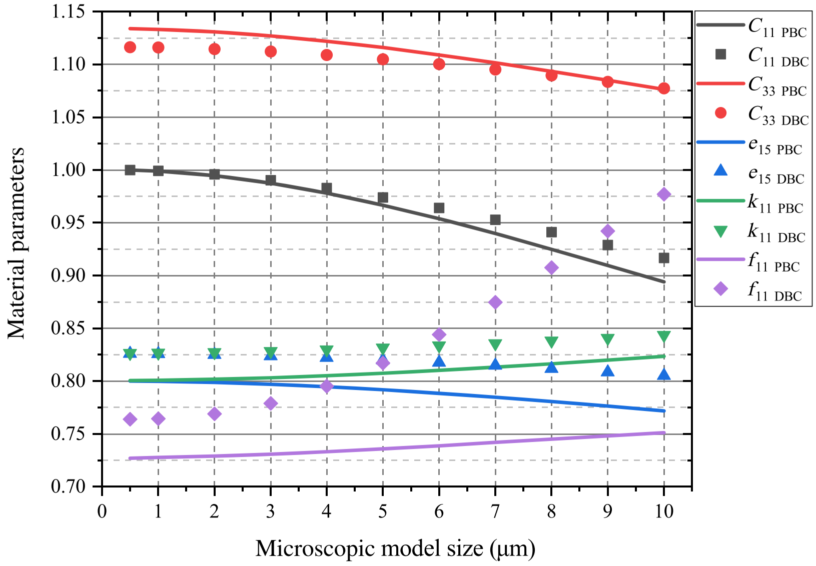

FIGURE 9 Material parameters of different microscopic model sizes with different boundary conditions.

of the considered boundary conditions, while the dielectric, piezoelectric, and flexoelectric coefficients differ noticeably under DBC.

Keeping the intrinsic length constant (1μm), the effects of microscale model size under PBC are shown in Figure 8. The elastic and piezoelectric coefficients decrease, while the dielectric and flexoelectric coefficients increase with the increase of microscale model size. It is noted that the effective elastic coefficients C_{11} and C_{33} decrease as the RVE size increases, which is consistent with the "smaller is stronger" phenomenon. On the other hand, the dielectric, piezoelectric, and flexoelectric coefficients are also larger under DBC compared to PBC, as in Figure 9.

5.1.2 | The effects of porosity and void distribution

The side length of the model and intrinsic length are 1 μm, and PBC is set as the boundary condition. The variation of the equivalent material parameters is linearly related to the porosity as shown in Figure 10. As the porosity increases, the

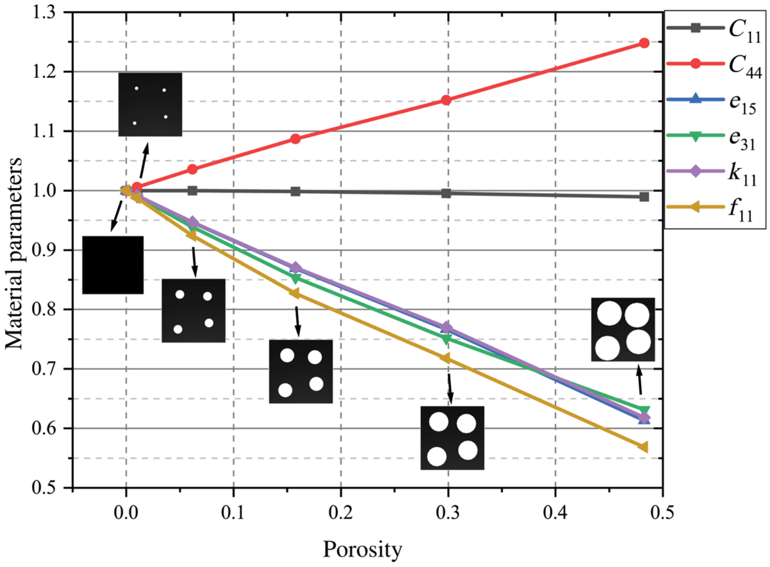

FIGURE 10 Material parameters of different porosities.

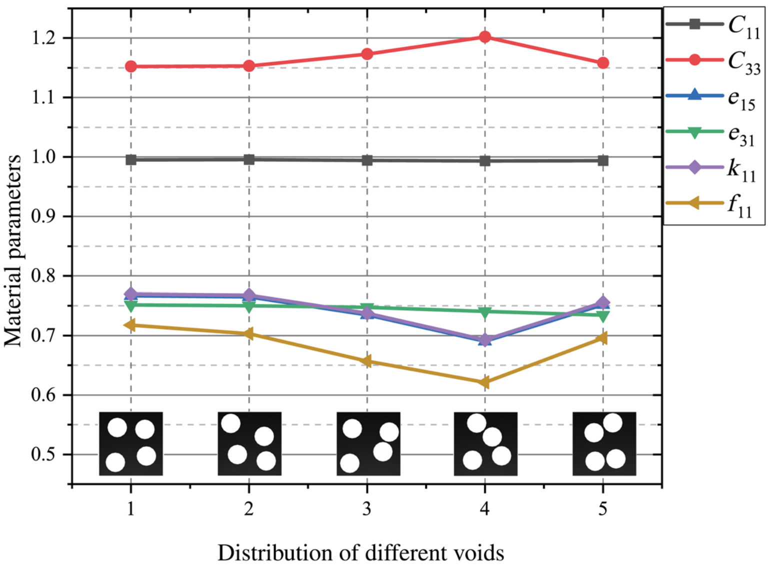

FIGURE 11 Material parameters of different distribution of holes.

dielectric, piezoelectric and flexoelectric coefficients decrease, and the elastic coefficient C_{33} increases, while the elastic coefficient C_{11} remains almost unchanged. It should be noted that when the porosity is zero, the equivalent material parameters are the same as the microscopic material, which is consistent with intuition. According to Figure 11, the equivalent flexoelectric parameter is more obviously impacted by the void distribution than other parameters. Compared with void distribution, the influence of shape and topology of microstructure on the equivalent material parameters will be greater, which needs further study.

5.2 | Creating materials with piezoelectric behavior without using piezoelectric materials

Flexoelectricity can be exploited to design piezoelectric effects without using piezoelectric materials by seeking to induce strain gradients.[7,49,50] One method is to introduce a triangular hole in a sheet, then a net nonzero polarization exists under

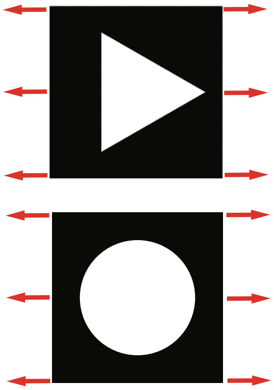

FIGURE 12 Piezoelectric nanocomposites without using piezoelectric materials.[49]

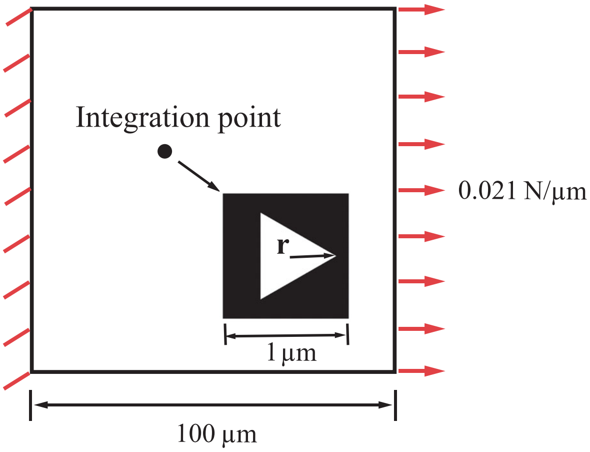

FIGURE 13 Macroscopic and microscopic models.

uniform stretching. It is to be noted that, the average polarization remains zero if the shape of the hole is circular, as shown in Figure 12. In this article, similar methods are applied in the microscale model to create equivalent piezoelectric coefficients in the absence of piezoelectric materials.

5.2.1 | Two-scale linear analysis of a uniaxial tensioned square plate

The macroscale model is a square plate subjected to uniaxial tension, and the microscale model is a square with a triangular hole in the center (Figure 13). The material properties are similar to the ones used in the previous examples as listed in Table 2, except that the values of piezoelectric coefficients are considered to be zero. The intrinsic length is set to be 1 μm.

The two-scale linear analysis is illustrated in Figure 14. The C^1 discretization scheme is used at both scales. The homogenization is performed at the microscale, where the equivalent material coefficients are set as the constitutive model for the macroscopic model. After solving the boundary value problems (BVP), the strain, strain gradient, and electric field of an integration point are applied on the RVE through the periodic boundary condition. The response of the RVE can be obtained by solving the BVP at the microscale.

Figure 15 gives piezoelectric coefficients with different hole sizes measured by the radius r of the inscribed circle of a triangle. The piezoelectric coefficients e_{11}, e_{12}, e_{23} generally increase as r increases, while e_{13}, e_{21}, e_{22} are almost zero. It is noteworthy that the equivalent piezoelectric coefficients are calculated to be zero when the hole is a circle, regardless of the hole size, which is consistent with the discussion in Reference 49.

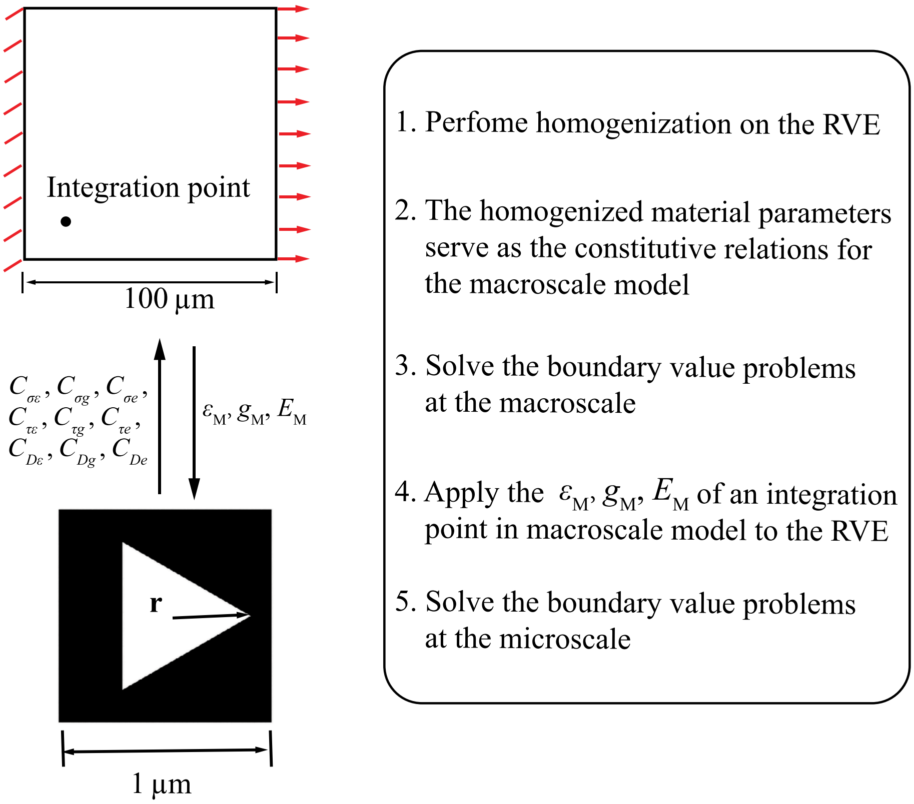

FIGURE 14 The procedures for the two-scale linear analysis.

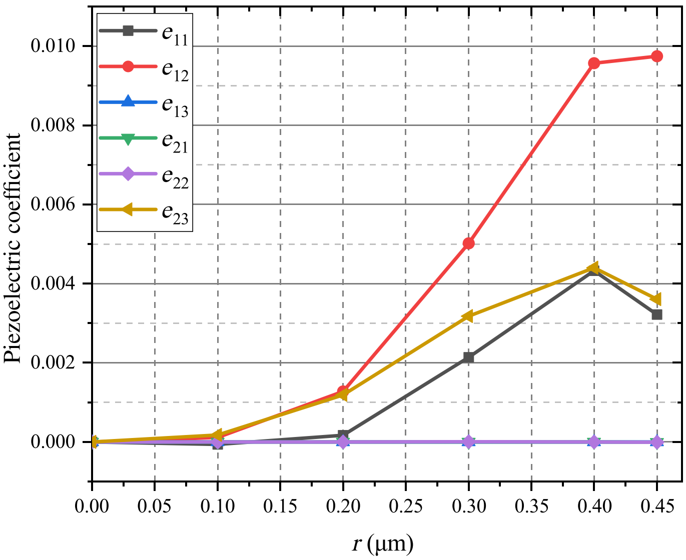

FIGURE 15 Equivalent piezoelectric coefficients (C/m^2) of different hole sizes.

The electric displacement field D_1 of the macro model with $r = 0.4\ \mu$m in the microstructure is shown in Figure 16. The macroscale model is a square plate subjected to uniaxial tension, resulting in a small strain gradient, and the piezoelectric coefficients are zero. In the Figure 16, D_1 is quite evident, indicating the apparent piezoelectric effect. The electric displacement field D_1 of the microstructure which corresponds to one integration point of element 1 in the macro model is also given in the figure. The calculation procedure has been described in Figure 3, and the macro-micro scale transition is carried out only once because of the linear elastic analysis.

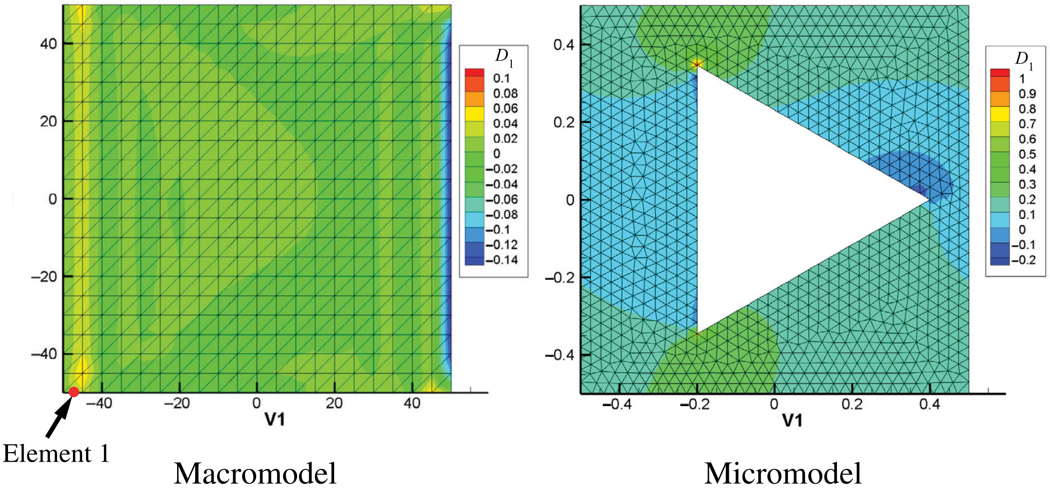

FIGURE 16 D_1 of the macroscale and microscale model (C/m^2).

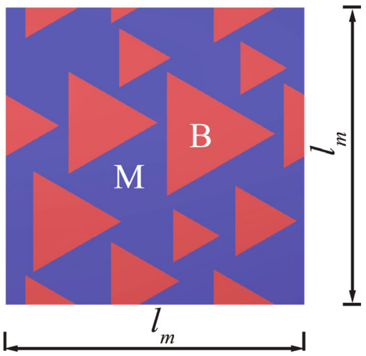

FIGURE 17 Flexoelectric composites.

5.2.2 | Creating piezoelectric materials with flexoelectric composites

Similarly, we can design piezoelectric materials with flexoelectric composites by distributing flexoelectric inclusions (B) in the dielectric matrix (M), as shown in Figure 17. The material properties of the inclusions are listed in Table 2, the side length l_m is 1 μm, and the intrinsic length is ignored. The dielectric coefficients of the matrix are the same as the inclusions, but the flexoelectric coefficients are zero. To induce the strain gradients, the elastic tensor of the matrix is adjusted and set to be the inclusions' elastic tensor multiplied by a factor less than 1. As the factor varies between 0 and 1, the homogenized piezoelectric coefficients vary as shown in Figure 18. when the factor is 1 or 0, the homogenized piezoelectric coefficients are nearly zero because the strain gradient is too small (factor = 1) or the connection between the inclusions is extremely weak (factor = 0). The ideal factor is around 0.2.

Moreover, the size-dependent behavior of flexoelectricity can be used to enhance the homogenized piezoelectric coefficients. By reducing the size of the microscale composite structure, from the micron-scale to the nanoscale, the homogenized piezoelectric coefficients increase significantly even though the elastic tensor factor is 1 (Figure 19). Interestingly, we can get similar results by increasing the flexoelectric coefficients of the inclusions without shrinking the microstructure size. The same homogenized piezoelectric coefficients can be obtained simply by increasing the flexoelectric coefficients of the inclusions by a factor of f_k (Figure 19), instead of scaling the microstructure down when regardless of the intrinsic length, which are consistent with the dimensional analysis. The results in Figure 19 illustrate the size-dependent behaviour of flexoelectricity in another way.

Remark: The self-consistency of the proposed method is reflected in four aspects: 1. The equivalent material parameters are the same as the microscopic material when the porosity is zero (Figure 11); 2. The equivalent piezoelectric

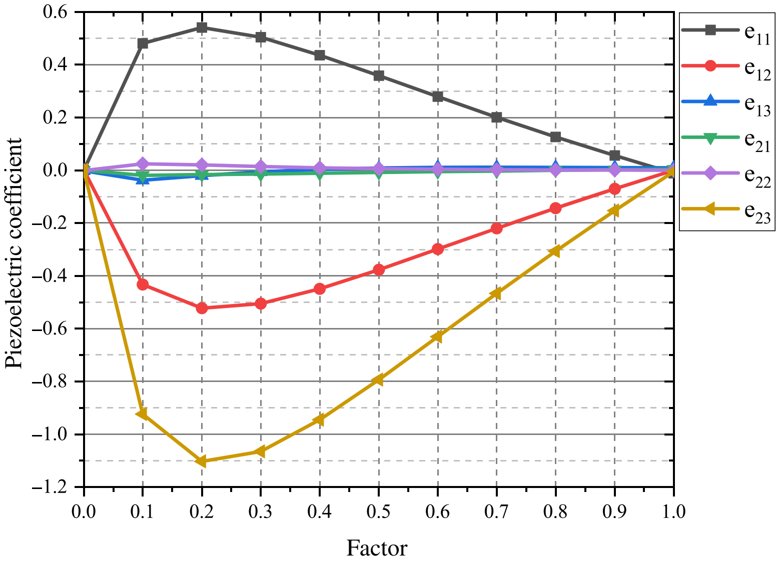

FIGURE 18 Homogenized piezoelectric coefficients (C/m^2) of different factors.

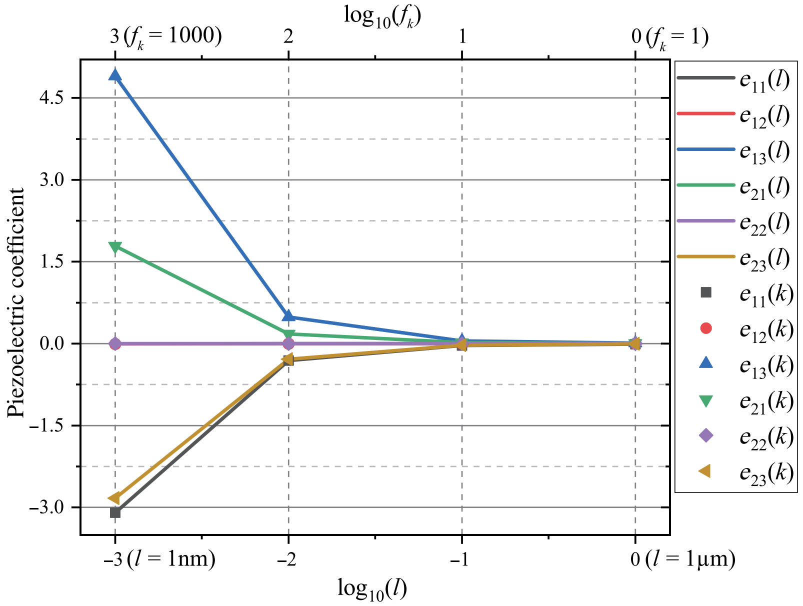

FIGURE 19 Homogenized piezoelectric coefficients (C/m^2) of different micromodel sizes l and factors f_k.

coefficients are calculated to be zero when the hole is a circle; 3. The homogenized piezoelectric coefficients are nearly zero when the elastic tensor factor of the matrix is 1 or 0 (Figure 18); 4. The same homogenized piezoelectric coefficients can be obtained by increasing the flexoelectric coefficients of the inclusions or shrinking the microstructure size (Figure 19).

6 | CONCLUSION

The computational second-order homogenization strategy of flexoelectric composites has been presented. The framework was implemented with C^1 triangular finite elements based on the secondary development of ABAQUS via user subroutines UEL and UVARM. Compared to the asymptotic expansion method, the homogenized electromechanical properties can be computed using perturbation analysis without complicated mathematical derivations. The influence of intrinsic length, micromodel size, and the two boundary conditions on the effective coefficients of flexoelectric microstructure are discussed. The influence of porosity and void distribution in the microstructure on the equivalent piezoelectric coefficients are also studied. The homogenized piezoelectric coefficients by introducing triangular voids or flexoelectric inclusions in the microstructure are determined. In this work, we restrict the computational second-order homogenization scheme to the linear two-dimensional analysis of the direct flexoelectricity. The Bell triangle element suffers from computational inefficiency and its extension to three-dimensional (3D) problems is cumbersome, while the IGA method is more suitable for solving 3D problems for flexoelectricity. Multiscale nonlinear and 3D problems with the IGA method will be explored in future research.

ACKNOWLEDGMENTS

This work is supported by the ERC Starting Grant COTOFLEXI (Grant No. 802205). The authors acknowledge the support from the Cluster of Excellence PhoenixD (EXC 2122, Project ID 390833453) at Leibniz University Hannover. Open Access funding enabled and organized by Projekt DEAL.

DATA AVAILABILITY STATEMENT

The data that support the findings of this study are available from the corresponding author upon reasonable request.

ORCID

Thomas Böhlke https://orcid.org/0000-0001-6884-0530

REFERENCES

1. Majdoub M, Sharma P, Cagin T. Enhanced size-dependent piezoelectricity and elasticity in nanostructures due to the flexoelectric effect. *Phys Rev B*. 2008;77(12):125424.
2. Nguyen TD, Mao S, Yeh Y-W, Purohit PK, McAlpine MC. Nanoscale flexoelectricity. *Adv Mater*. 2013;25(7):946-974.
3. Zubko P, Catalan G, Tagantsev AK. Flexoelectric effect in solids. *Annu Rev Mat Res*. 2013;43(1):387-421.
4. Yudin P, Tagantsev A. Fundamentals of flexoelectricity in solids. *Nanotechnology*. 2013;24(43):432001.
5. Wang B, Gu Y, Zhang S, Chen L-Q. Flexoelectricity in solids: Progress, challenges, and perspectives. *Prog Mater Sci*. 2019;106:100570.
6. Arias I, Catalan G, Sharma P. The emancipation of flexoelectricity. 2022.
7. Mocci A, Barceló-Mercader J, Codony D, Arias I. Geometrically polarized architected dielectrics with apparent piezoelectricity. *J Mech Phys Solids*. 2021;157:104643.
8. Zhang C, Zhang L, Shen X, Chen W. Enhancing magnetoelectric effect in multiferroic composite bilayers via flexoelectricity. *J Appl Phys*. 2016;119(13):134102.
9. Zhang M, Yan D, Wang J, Shao L-H. Ultrahigh flexoelectric effect of 3d interconnected porous polymers: modelling and verification. *J Mech Phys Solids*. 2021;151:104396.
10. McBride A, Davydov D, Steinmann P. Modelling the flexoelectric effect in solids: a micromorphic approach. *Comput Methods Appl Mech Eng*. 2020;371:113320.
11. Guinovart-Sanjuán D, Merodio J, López-Realpozo JC, et al. Asymptotic homogenization applied to flexoelectric rods. *Materials*. 2019;12(2):232.
12. Mohammadi P, Liu L, Sharma P. A theory of flexoelectric membranes and effective properties of heterogeneous membranes. *J Appl Mech*. 2014;81(1):011007.
13. Sharma N, Maranganti R, Sharma P. On the possibility of piezoelectric nanocomposites without using piezoelectric materials. *J Mech Phys Solids*. 2007;55(11):2328-2350.
14. Mawassy N, Reda H, Ganghoffer J-F, Eremeyev VA, Lakiss H. A variational approach of homogenization of piezoelectric composites towards piezoelectric and flexoelectric effective media. *Int J Eng Sci*. 2021;158:103410.
15. Yvonnet J, Chen X, Sharma P. Apparent flexoelectricity due to heterogeneous piezoelectricity. *J Appl Mech*. 2020;87(11):111003.
16. Chen X, Yvonnet J, Park H, Yao S. Enhanced converse flexoelectricity in piezoelectric composites by coupling topology optimization with homogenization. *J Appl Phys*. 2021;129:245104.
17. Chen X, Yvonnet J, Yao S, Park H. Topology optimization of flexoelectric composites using computational homogenization. *Comput Methods Appl Mech Eng*. 2021;381:113819.
18. Geers M, Yvonnet J. Multiscale modeling of microstructure–property relations. *MRS Bull*. 2016;41(8):610-616.
19. Geers MG, Kouznetsova VG, Brekelmans W. Multi-scale computational homogenization: trends and challenges. *J Comput Appl Math*. 2010;234(7):2175-2182.
20. Kaczmarczyk Ł, Pearce CJ, Bićanić N. Scale transition and enforcement of rve boundary conditions in second-order computational homogenization. *Int J Numer Methods Eng*. 2008;74(3):506-522.
21. Kouznetsova V, Geers MG, Brekelmans W. Multi-scale second-order computational homogenization of multi-phase materials: a nested finite element solution strategy. *Comput Methods Appl Mech Eng*. 2004;193(48–51):5525-5550.

22. Lesičar T, Tonković Z, Sorić J. A second-order two-scale homogenization procedure using c^1 macrolevel discretization. *Comput Mech*. 2014;54(2):425-441.
23. Lesičar T, Sorić J, Tonković Z. Large strain, two-scale computational approach using c1 continuity finite element employing a second gradient theory. *Comput Methods Appl Mech Eng*. 2016;298:303-324.
24. Lesičar T, Tonković Z, Sorić J. Two-scale computational approach using strain gradient theory at microlevel. *Int J Mech Sci*. 2017;126:67-78.
25. Lesičar T. *Multiscale Modeling of Heterogeneous Materials Using Second-Order Homogenization*. PhD thesis, University of Zagreb. Faculty of Mechanical Engineering and Naval Architecture. 2015.
26. Ghasemi H, Park HS, Rabczuk T. A level-set based iga formulation for topology optimization of flexoelectric materials. *Comput Methods Appl Mech Eng*. 2017;313:239-258.
27. Nanthakumar S, Zhuang X, Park HS, Rabczuk T. Topology optimization of flexoelectric structures. *J Mech Phys Solids*. 2017;105:217-234.
28. Deng F, Deng Q, Yu W, Shen S. Mixed finite elements for flexoelectric solids. *J Appl Mech*. 2017;84(8):081004.
29. Mao S, Purohit PK, Aravas N. Mixed finite-element formulations in piezoelectricity and flexoelectricity. *Proc R Soc A Math Phys Eng Sci*. 2016;472(2190):20150879.
30. Poya R, Gil AJ, Ortigosa R, Palma R. On a family of numerical models for couple stress based flexoelectricity for continua and beams. *J Mech Phys Solids*. 2019;125:613-652.
31. He B, Javvaji B, Zhuang X. Characterizing flexoelectricity in composite material using the element-free galerkin method. *Energies*. 2019;12(2):271.
32. Yvonnet J, Liu L. A numerical framework for modeling flexoelectricity and maxwell stress in soft dielectrics at finite strains. *Comput Methods Appl Mech Eng*. 2017;313:450-482.
33. Dasgupta S, Sengupta D. A higher-order triangular plate bending element revisited. *Int J Numer Methods Eng*. 1990;30(3):419-430.
34. Maranganti R, Sharma N, Sharma P. Electromechanical coupling in nonpiezoelectric materials due to nanoscale nonlocal size effects: Green's function solutions and embedded inclusions. *Phys Rev B*. 2006;74(1):014110.
35. Sharma N, Landis C, Sharma P. Piezoelectric thin-film superlattices without using piezoelectric materials. *J Appl Phys*. 2010;108(2):024304.
36. Abdollahi A, Millán D, Peco C, Arroyo M, Arias I. Revisiting pyramid compression to quantify flexoelectricity: A three-dimensional simulation study. *Phys Rev B*. 2015;91(10):104103.
37. Shen S, Hu S. A theory of flexoelectricity with surface effect for elastic dielectrics. *J Mech Phys Solids*. 2010;58(5):665-677.
38. Hu S, Shen S. Variational principles and governing equations in nano-dielectrics with the flexoelectric effect. *Sci China Phys Mech Astron*. 2010;53(8):1497-1504.
39. Hill R. Elastic properties of reinforced solids: some theoretical principles. *J Mech Phys Solids*. 1963;11(5):357-372.
40. Schröder J, Keip M-A. Two-scale homogenization of electromechanically coupled boundary value problems. *Comput Mech*. 2012;50(2):229-244.
41. Hrabok M, Hrudey T. A review and catalogue of plate bending finite elements. *Comput Struct*. 1984;19(3):479-495.
42. Argyris JH, Fried I, Scharpf DW. The tuba family of plate elements for the matrix displacement method. *Aeronaut J*. 1968;72(692):701-709.
43. Bell K. A refined triangular plate bending finite element. *Int J Numer Methods Eng*. 1969;1(1):101-122.
44. Zervos A, Papanastasiou P, Vardoulakis I. A finite element displacement formulation for gradient elastoplasticity. *Int J Numer Methods Eng*. 2001;50(6):1369-1388.
45. Zervos A, Papanicolopulos S-A, Vardoulakis I. Two finite-element discretizations for gradient elasticity. *J Eng Mech*. 2009;135(3):203-213.
46. Manzari MT, Yonten K. C1 finite element analysis in gradient enhanced continua. *Math Comput Model*. 2013;57(9–10):2519-2531.
47. Zhuang X, Nguyen BH, Nanthakumar SS, Tran TQ, Alajlan N, Rabczuk T. Computational modeling of flexoelectricity—a review. *Energies*. 2020;13(6):1326.
48. Aifantis EC. Gradient aspects of crystal plasticity at micro and macro scales. *Key Engineering Materials*. Vol 177. Trans Tech Publ; 2000:805.
49. Krichen S, Sharma P. Flexoelectricity: a perspective on an unusual electromechanical coupling. *J Appl Mech*. 2016;83(3):030801.
50. Deng Q, Liu L, Sharma P. Flexoelectricity in soft materials and biological membranes. *J Mech Phys Solids*. 2014;62:209-227.

How to cite this article: Zhuang X, Li B, Nanthakumar SS, Böhlke T. Second-order computational homogenization of flexoelectric composites. *Int J Numer Methods Eng*. 2025;126(1):e7598. doi: 10.1002/nme.7598